An empirical model of electron and ion fluxes derived from observations at geosynchronous orbit

M. H. Denton[1], M. F. Thomsen[2], V. K. Jordanova[3], M. G. Henderson[3], J. E. Borovsky[1], J. S. Denton[4], D. Pitchford[5], and D. P. Hartley[6].

1. Center for Space Plasma Physics, Space Science Institute, CO 80301, USA.
2. Planetary Science Institute, AZ 85719, USA.
3. ISR-1, Los Alamos National Laboratory, NM 87545, USA.
4. Analytical Services, Sellafield Ltd., Seascale, UK.
5. SES Engineering, L-6815 Château de Betzdorf, Luxembourg.
6. Department of Physics, Lancaster University, LA1 4YB, UK.

ABSTRACT

Knowledge of the plasma fluxes at geosynchronous orbit is important to both scientific and operational investigations. We present a new empirical model of the ion flux and the electron flux at geosynchronous orbit (GEO) in the energy range ~1 eV to ~40 keV. The model is based on a total of 82 satellite-years of observations from the Magnetospheric Plasma Analyzer instruments on Los Alamos National Laboratory satellites at GEO. These data are assigned to a fixed grid of 24 local-times and 40 energies, at all possible values of Kp. Bi-linear interpolation is used between grid points to provide the ion flux and the electron flux values at any energy and local-time, and for given values of geomagnetic activity (proxied by the 3-hour Kp index), and also for given values of solar activity (proxied by the daily F10.7 index). Initial comparison of the electron flux from the model with data from a Compact Environmental Anomaly Sensor II (CEASE-II), also located at geosynchronous orbit, indicate a good match during both quiet and disturbed periods. The model is available for distribution as a FORTRAN code that can be modified to suit user-requirements.

1. Introduction

Geosynchronous orbit (GEO) is located at the approximate boundary between the inner magnetosphere (where plasma motion is largely dominated by co-rotation and gradient-curvature drift), and the outer magnetosphere (where plasma motion is largely dominated by the global magnetospheric convection cycle). Many scientific models of the plasma populations in the inner magnetosphere use the ion and electron parameters at GEO as inputs or boundary conditions [e.g., *Jordanova et al.*, 1998; 2003]. From an operational perspective, GEO is one of the most popular locations for satellite hardware since the orbital period of 24 hours ensures that satellites remain at the same geographic longitude, and co-rotate along with the Earth. Over 400 satellites, used for communications, scientific, and military purposes, are currently on-orbit at GEO (e.g. http://www.satsig.net/sslist.htm) at an equatorial distance of 6.6 Earth radii (R_E). Knowledge of the particle flux environment at GEO is important when designing and operating such satellites.

In light of the importance of GEO, both scientifically and operationally, the plasma environment in this region is of great interest. We present here a new model of the flux of electrons and ions at GEO, for energies between ~1 eV and ~40 keV, as a function of local-time, energy, geomagnetic activity, and solar activity. This energy range encompasses the plasmasphere, the electron plasma sheet, the ion plasma sheet, and the substorm-injected supra-thermal tails of both the electron and ion plasma sheets. Each of these populations is encountered regularly by satellites on station at GEO.

The aim in developing a new model of the plasma environment at GEO is to complement existing models such as AP9/AE9/SPM [*Ginet et al.*, 2014], IGE-2006 [*Sicard-Piet et al.*, 2008] or the two-Maxwellian ATS-6 models [*Purvis et al.*, 1984]. Such models tend to be tailored towards spacecraft operators and the operational community, and concerned primarily with hardware effects due to the harsh electron and ion flux environment (e.g. internal charging, total dose over mission lifetime). Other, scientific models such as the IMPTAM model of *Ganushkina et al.* [2013; 2015] follow distributions of ions and electrons from the tail plasma sheet to the inner magnetosphere by careful consideration of the physics in the region. In the current study, an empirical model that utilizes the large data-sets that have been gathered over more than two full solar-cycles is developed, with respect to a limited energy range. With this range the model address a range of variables that affect the ion flux and the electron flux. This first version of the model addresses the variation of the ion and electron fluxes with respect to local time, energy, geomagnetic activity, and solar activity.

The primary dataset that underpins this new model is the largest collection of calibrated electron and ion fluxes from GEO in existence, namely the series of measurements made by Los Alamos National Laboratory (LANL) satellites. The aim of the model is to focus on a limited number of energies, at the lower-end of the AP9/AE9 range. By concentrating on a single spatial location (GEO), it is possible to use the breadth of the dataset to allow statistical investigation of the effects of various solar wind and geophysical parameters upon the plasma populations in this region. The size of the LANL database means it is possible to model the fluxes as a function of geomagnetic-activity, solar-activity, local-time, and energy, and hence more-accurately describe the behavior of these fluxes. In future it is hoped that the model will be extended to allow users to predict the flux at GEO as a function of other variables such as the solar wind velocity, magnetic field orientation, and number density.

2. Observations

The ion and electron populations at GEO are routinely measured by Magnetospheric Plasma Analyzer (MPA) instruments on-board multiple LANL satellites [*Bame et al.*, 1993]. The full

MPA dataset extends from 1989 to the present, covering more than two full solar cycles (~100 satellite-years of data). MPA instruments are electrostatic analyzers that measure the three-dimensional energy-per-charge distributions of both ions and electron between ~1 eV/q and ~40 keV/q [*Bame et al.*, 1993; *Thomsen et al.*, 1999]. The time cadence of the observations is such that a single ten second snapshot of the distributions is available for analysis every 86 seconds. In contrast to many other scientific satellites, the LANL spacecraft platform is particularly well-suited to observations of thermal ions since the spacecraft charges slightly negatively with respect to infinity. Thus, all low-energy ions are readily detected at all times, typically accelerated towards the spacecraft by the spacecraft potential. In contrast, electrons moving towards the spacecraft are decelerated (or totally repelled) by the negative potential [*Thomsen et al*. 1999]. Although there are no magnetometers on-board the LANL satellites, the magnetic-field direction can be derived from the symmetry axis of the three-dimensional particle distributions, allowing identification of the components of the temperature parallel and perpendicular to the field [*Thomsen et al.*, 1999].

With respect to the low-energy ion population (<100 eV), MPA instruments regularly observe ions in the co-rotating plasmasphere during extended periods of calm geomagnetic activity [*Thomsen et al.*, 1998; *Denton et al.*, 2005; *Denton and Borovsky*, 2008; *Borovsky and Denton*, 2009]. MPA instruments also measure thermal ions in plasmaspheric drainage plumes during instances of erosion [*Elphic et al.*, 1996; *Weiss et al.*, 1997; *Goldstein et al.*, 2004; *Denton and Borovsky*, 2008] and the return of cold ions to GEO during plasmaspheric refilling events [*Thomsen et al.*, 1998; *Lawrence et al.*, 1999; *Su et al.*, 2001; *Sandel and Denton*, 2007; *Borovsky and Denton*, 2008; *Borovsky et al.*, 2013; 2014; *Denton and Borovsky*, 2014].

MPA instruments also measure the medium-energy population (~100 eV to 40 keV) of the ion plasma sheet and the electron plasma sheet (e.g. *Borovsky et al.* [1997]; *Thomsen et al.* [1998, 2003, 2007]; *Korth et al.* [1999]; *Denton et al*. [2005; 2009]). These plasmas are typically delivered into the inner magnetosphere, on drift paths that originate on the nightside of the Earth, at distances >6.6 R_E. During enhanced magnetospheric convection intervals, electrons and ions drift inwards, crossing GEO close to local midnight (e.g. *Thomsen et al.* [2001], *Denton et al.* [2007]), and subsequently drift either eastwards or westwards around the Earth, following drift-paths that are charge-dependent and energy-dependent (e.g. *Korth et al.* [1999]). However, the process by which the plasma actually arrives close to GEO is likely associated with particle injections [*Mauk and Meng*, 1983] such as occur during substorms [*Henderson et al.*, 2006a; 2006b].

In this study observations of the plasma flux, made by MPA instruments on seven satellites between 1990 and 2007, are analyzed. A plot of the cumulative number of years of data utilized in this study, and the distribution of the data amongst individual satellites, is shown in Figure 1, along with the distribution of data from each satellite as a function of year. In total, 82 satellite-years of observations are used in this study. The ion and electron flux distributions from LANL/MPA are analyzed with respect to energy, local-time, geomagnetic activity, and solar activity, with the ultimate outcome being a model of the flux of ions and electrons at all energies between ~1 eV and ~40 keV, and at all local-times.

Example plots of the ion and electron fluxes as a function of local-time during a 24-hour period of time are provided in Figure 2. The top panel of Figure 2 shows the observed ion flux during 30th December 2001 measured by LANL/MPA. The spacecraft encounters a plasmaspheric drainage plume between ~4-8 UT and, except for this period, resides in a low-density plasma-sheet environment for the rest of the day. Note, the low energy ions in the plasmaspheric plume (< 1 eV) are accelerated to ~10 eV by the negative spacecraft potential. The bottom panel of Figure 2 shows the electron flux during 30th December 2001 measured by LANL/MPA. The spacecraft resides in the electron plasma-sheet for most of this day except between ~4-8 UT. The high fluxes seen prominently in the low-energy electron channels (<40 eV) are dominated by photo-electrons produced at the spacecraft and should be disregarded.

3. Analysis

Earlier studies using the LANL/MPA dataset have examined the variation in ion flux and electron flux over more than a full solar cycle [*Thomsen et al.* 2007]. The average fluxes for ions and electrons for each year from 1990 to 2004 have been tabulated (along with percentile flux limits) with the aim of providing users with useful information with which to guide satellite design and testing. The purpose of the current study is to extend the work carried out by *Thomsen et al.* [2007] in order to generate a predictive model of the variations in both the ion flux and the electron flux, at specific energies, with respect to a selection of geophysical parameters. Rather than tabulated values of ion flux and electron flux at a selection of pre-determined energies, here the aim is a model that can provide the fluxes at all values of energy and local-time, as a function of geomagnetic and solar activity. By following similar methodology to that successfully utilized in previous statistical studies of the LANL/MPA data (e.g. *Korth et al.* [1999], *Denton et al.* [2005; 2012], *Thomsen et al.* [2011], *Borovsky and Denton* [2006], *MacDonald et al.* [2008; 2010]), the average variation of the measured ion and electron fluxes for a variety of conditions can be determined.

As demonstrated by *Thomsen et al.* [2007] the ion and electron fluxes measured by the seven LANL/MPA instruments agree within ~20%, indicating good calibration between satellites. Hence it is appropriate to combine the measurements over the entire database from all satellites, during all years. However, we don not use ion data from spacecraft 1989-046 after January 2000 because of an intermittent instrument problem that began then. The data-analysis technique used in this current study can be summarized as follows: (1) Assign each individual data point from each satellite to the appropriate bin in a grid of 40 energies (evenly-spaced logarithmically from ~1 eV to ~40 keV) and 24 local-times, for each of the 28 values of Kp; (2) calculate the mean, median, standard deviation, and the 5^{th}, 25^{th}, 75^{th} and 95^{th} percentiles in each bin where there are more than 5 individual data points; (3) interpolate between the bins using bi-linear interpolation to provide the electron flux and the ion flux at all values of local-time and energy, at a fixed Kp. Note, when calculating the mean of the values, the log of each value is taken first, then the mean of all logged values is calculated.

Three salient points are worthy of note regarding the analysis: (i) Magnetosheath intervals are identified and removed from all averaging. At times, when the solar wind pressure is very high, the magnetopause may move inwards of GEO, and then LANL satellites will then reside in the magnetosheath. Such intervals are removed from the analysis by only considering data where the hot ion density (calculated from the moments of the full ion distribution) is less than 5.0 cm^{-3} and the perpendicular ion temperature is greater than 2000 eV [*Thomsen et al.*, 1999; *Denton et al.*, 2005]. These criteria have been used in numerous previous studies to good effect (e.g. [*Korth et al.* [1999], *Denton et al.* [2005]). (ii) Since each MPA instrument has slightly different channel edge energies, the energy values quoted for the average fluxes below will differ slightly depending on exactly how many data-points from each satellite contribute to the averages. To allow for this, the energies quoted in figures and tables below relate to the averaged centre-energy from each satellite, weighted by the number of satellite-years of data from each satellite contributing to the averages. The full list of edge-energies for the MPA instruments used in this study may be found in *Thomsen et al.* [1999]. (iii) At times, particularly in eclipse, the LANL spacecraft may charge very strongly negative (1000s of volts) (see the appendix of *Denton and Borovsky* [2012] for a discussion of the variation of the spacecraft potential as a function of local-time and Kp). Although a robust methodology is implemented to correct the ion and electron fluxes for all values of the spacecraft potential [*Thomsen et al.*, 1999], in the current study all periods when the measured potential is extremely negative (< -500 V) are not included in the analysis. Note: since the periods of greatest negative charging typically occur for the highest values of Kp, close to local midnight (when the fluxes are most enhanced) the average fluxes for these periods are likely to be slightly under-estimated.

3.1 Probability distributions of flux measurements

Figure 3 contains plots of the probability distribution of the electron flux (left column) and the ion flux (right column) at three example energies (~18 keV, ~2 keV, and ~300 eV), corresponding to the 4^{th}, 11^{th}, and 18^{th} energy channels of the LANL/MPA instrument. These distributions pertain to all data taken between 1990 and 2007 (a total of 82 satellite-years of data), following the analysis technique described above (i.e. sheath intervals and periods of very strong spacecraft surface charging are not included in the analysis). Statistical parameters for these distributions are given in Table 1. For the electrons at ~18 keV and ~2 keV, it is clear that a double-peaked distribution exists, and investigation reveals that these two peaks relate to periods when the spacecraft are either inside or outside the electron plasma sheet (also compare with Figure 5, left column). For the electrons at ~300 eV, the probability distribution of possible flux values has a single peak, with an extended tail at lower flux values. In contrast to the electrons, the ion flux at all three energies shown appears to be single-peaked.

3.1 Energy, local-time, and geomagnetic activity

Figure 4 contains example results obtained by analyzing the LANL/MPA observations with respect to energy, local-time, and geomagnetic activity, using the technique described above. The top row shows the mean electron flux and the mean ion flux, averaged over the entire MPA dataset for all intervals where the instantaneous Kp index [*Bartels et al.*, 1939] is equal to 2. Kp is utilized since it is known to be a very good proxy for large-scale magnetospheric convection [*Thomsen*, 2004] and a good indicator of general geomagnetic activity, as well as being a parameter that is available to users almost instantaneously (e.g. from the NOAA Space Weather Prediction Center). The bottom row of Figure 4 shows the same data as the top row, but now plotted as a three-dimensional surface to better reveal to the reader the relative variations in each parameter. It is clear from Figure 4 (and as shown in previous studies) that both the ion flux and the electron flux display well-ordered variations with local-time. Examination of the plots for all other Kp values demonstrates that the fluxes are also well-ordered with the Kp index. *Korth et al.* [1999] demonstrated that the observed patterns of electron and ion fluxes measured by LANL/MPA at geosynchronous orbit can be well-explained in terms of the particle energy, and the balance between the co-rotation electric field and the convection electric field proxied by Kp [*Korth et al.*, 1999; *Korth and Thomsen*, 2001]. For energies greater than ~100 eV, which are typical of the plasma sheet, the electrons (that come from the plasma sheet at distances > 6.6 R_e) first arrive at GEO on the nightside of the Earth, close to local midnight, and drift to the east. The corresponding plasma sheet ions first arrive at GEO close to local midnight and drift to the west. Both electrons and ions are susceptible to energisation and loss processes as they drift [*Korth et al.*, 1999].

The mean electron flux shown in Figure 4 is well-ordered with respect to energy and local-time and varies by over six orders of magnitude (over the full-range of possible Kp values – figures not shown). In general the greatest measured electron fluxes are found at the lowest energies. However, as discussed above, these fluxes are dominated by spacecraft-produced photoelectrons reaching the MPA detector owing to differential spacecraft charging. Thus the electron fluxes below ~40 eV should be ignored. For energies above ~100 eV it is clear that the electron flux is both energy-dependent and local-time dependent, with the greatest electron flux observed in the dawn region.

The mean ion flux also shows a well-ordered structure, which varies by around five orders of magnitude over the full range of possible Kp values (figures not shown). The highest fluxes are found at the lowest energies (~10 eV) and correspond to thermal ions from the plasmasphere and from plasmaspheric drainage plumes.

Figure 5 contains plots of the mean electron flux and the mean ion flux for three levels of geomagnetic activity, proxied by the Kp index: Kp=0 (top row), Kp=3 (middle row), and Kp=6 (bottom row). These levels correspond to periods of very low activity (weak convection), moderate activity (moderate convection), and high activity (strong convection), respectively. These figures contain a wealth of detail into the morphology of the plasma environment at GEO, as a function of energy, local-time, and geomagnetic activity. Note in the three ion-flux plots in Figure 5 the dark (low-flux) "lane" in the higher-energy ions on the dayside. This dark lane represents the separation between ions that travel from the nightside to the dayside around the dawnside of the Earth versus around the duskside of the Earth. The total electric field of interest, **E**, is a combination of the co-rotation electric field and the cross-tail convection electric field. Lower-energy ions tend to follow $\mathbf{E}\times\mathbf{B}$ drift paths - with co-rotation these paths carry ions from the nightside around dawnside to the dayside; higher-energy ions tend to follow gradient-and-curvature drift paths - these paths carry ions from the nightside around dusk to the dayside. Ions that are near the energy that separates the dawnward versus duskward paths penetrate deep into the dipole and suffer strong charge-exchange losses with the hydrogen geocorona: hence the low-flux lane on the dayside. Similarly, the electron flux is reduced on the dayside due to the strong scattering loss by plasma waves for eastward drifting electrons [e.g. *Jordanova et al.*, 2010a]. Again, due to domination by spacecraft-produced photoelectrons, the electron fluxes below ~40 eV should be ignored.

From the examples shown in Figure 4 and Figure 5, and from equivalent plots for all other possible values of the Kp index, it is clear that the average electron and ion fluxes vary in a well-ordered (but also locally-complex) manner with respect to local-time, energy, and geomagnetic activity. In order to construct a model for the user community that is relatively simple and straight-forward, whilst also capturing the variations in the fluxes shown in Figure 4 and Figure 5, simple bi-linear interpolation is used to obtain values of the electron flux and the ion flux at locations between the cells, for any value of Kp and/or local-time. Thus, using the model created from these data, a user may specify any value of local-time and energy and be provided with an estimate of the electron flux and the ion flux.

3.2 Solar EUV flux variations

The solar EUV flux incident on the Earth's upper atmosphere causes the formation of an ionosphere with a peak number density of electrons and ions usually found at an altitude of ~300 km. It is well-established that outflow from the ionosphere is the source of a variable proportion of the plasma observed at GEO, both at low energies (plasmasphere) and at higher energies (plasma sheet) (e.g. *Borovsky et al.* [1997]; *Yau and Andre* [1997]; *Nose et al.* [2003]; *Huddleston et al.* [2005]; *Mouikis et al.* [2010]; *Welling and Ridley* [2010]; *Kronberg et al.* [2014]). Since the solar EUV flux is not constant, but changes both as a function of the solar rotation period (~27 days) and over the solar-cycle (~11 years), the number density of both ions and electrons in the upper atmosphere also varies over these (and other) timescales. A reasonably good proxy for solar EUV radiation is the F10.7 index – a measure of the flux of incident radiation with a wavelength of 10.7 cm – and also an index which is closely correlated with sunspot number.

Previous work utilizing the LANL/MPA dataset has shown that the fluxes of ions and of electrons at GEO are also strongly correlated with solar cycle – an unsurprising result if one assumes that a proportion of the plasma sheet ultimately originates from the thermal plasma of the ionosphere. *Denton et al.* [2005] showed that the electron number density (computed from the moments of the full LANL/MPA distributions) varied by roughly a factor of two over a solar cycle. *Thomsen et al.* [2007] further revealed the details of such changes by determining the average ion flux and electron flux, as a function of energy, with respect to the solar cycle. At low energies (<~50 eV) the ion flux is higher at solar minimum than at solar maximum, by a factor in excess of two. At higher energies (> ~50 eV) the situation is reversed and the ion flux at solar maximum is at least double that at solar minimum. The electron flux at these energies is also greatest at solar maximum, with a factor of at least two difference between solar minimum and solar maximum (see *Thomsen et al.* [2007]).

Although a fine-grained study of changes in the plasma populations at GEO at all points over a solar-cycle is beyond the scope of this current study, it is possible to achieve a coarse parameterization using three different ranges of the F10.7 index. Figure 6 contains plots of the averaged electron flux (left column) and averaged ion flux (right column) for low solar activity (F10.7 < 100 : top row), moderate solar activity (100 ≤ F10.7 < 170 : middle row) and high solar activity (F10.7 ≥ 170 : bottom row), during all intervals where Kp=2. Although differences between the ion flux and electron flux over the three levels of solar activity at a fixed energy are observed, these differences are typically much lower than the changes that occur as a function of geomagnetic activity and local-time. The differences are typically of the order of a factor of two, in agreement with the findings from earlier studies [*Denton et al.*, 2005; *Thomsen et al.*, 2007].

It should be noted that for very high values of the Kp index (Kp > ~7) there is an inadequate volume of data to completely fill the 40×24 grid of local-times and energies. In these instances it is straight-forward for a user to fall back to the version of the model where all data are included, regardless of the level of the F10.7 index. Example model outputs are contained in Table 2.

4. Model performance

4.1 Model comparison with MPA observations

Although comparing a model with a selection of the data used in construction of the model can be misleading, it may also give a useful indication of how well matched the model results are to observations during particular intervals. A comparison of the model output with observations from the MPA instrument on-board satellite 1994-084, during a representative five day period in 1999, can be found in Figure 7, along with a plot of the Kp index during this period. The period over which the comparison takes place is noteworthy in that it encompasses calm geomagnetic conditions, as well as very active conditions. Due to the high Kp values during this interval, the model used in the comparison does not consider F10.7 variations.

The top panel of Figure 7 shows the measured and the modeled electron flux at an energy of 1.545 keV. The solid blue line is the mean calculated from the model and the purple line is the median. The dashed lines are the 5^{th}, 25^{th}, 75^{th} and 95^{th} percentiles. In general the model tracks the general trend of the observations reasonably well during this period. The model does not capture sudden and sharp changes in the measured electron flux. The middle panel of Figure 7 shows the measured and modeled ion flux at an energy of 1.629 keV. The solid red line is the mean calculated from the model and the orange line is the median. The dashed lines are the 5^{th}, 25^{th}, 75^{th} and 95^{th} percentiles. As with the electrons, the model tracks the observations reasonably well during this period but does not capture sudden and sharp changes in the measured ion flux. Model performance at other energies in the MPA range is similar, with the model capturing the general trend of the measured fluxes, but not capturing any sharp changes in flux occurring over a short timescale. Following the same methodology used by *Ganushkina et al.* [2015] to compare between model and observed values we calculate the normalized root-mean-squared deviation (NRMSD) between the model predictions and the measured fluxes. Here the NRMSD values for electrons and ions during the five day period in Figure 7 are 0.975 and 1.873, respectively. Values below unity indicate the average error during the period in question is within a single standard deviation. Here, it is clear that (at these energies), the electron predictions are better matched to observations than the ion predictions.

4.2 Independent testing of the electron flux predictions

An independent test of the electron flux from the model has been performed in comparison with data gathered by a different satellite on-orbit at GEO. The AMC-12 satellite carries a Compact Environmental Anomaly Sensor II (CEASE-II) instrumentation package that measures the electron distribution from ~1 keV to ~ 45 keV. A full description of the CEASE-II package can be found in *Dichter et al.* [1998]. Previous comparison of the CEASE-II data from AMC-12 with a complex theoretical model during isolated substorms has been carried out by *Ganushkina et al.* [2014] who found generally good agreement between model predictions and observations when substorm-associated electromagnetic fields are taken into account.

Figure 8 shows a comparison between the electron flux measured at the AMC-12 satellite and the electron flux predicted by the model, during a five day period in 2013, along with a plot of the Kp index. The period over which the comparison takes place is noteworthy in that it encompasses calm geomagnetic conditions, as well as active conditions. The format of the figure is the same as that used in Figure 7.

The top panel of Figure 8 shows the comparison between model and observations at an energy of 13.40 keV. The model fluxes track the trend of the measured fluxes reasonably well during the first two days. In the following days as Kp increases the model fluxes also increase, and become somewhat higher than those actually observed. During this period the general trend in the model fluxes is similar to that in the observations. The measured flux is almost always within the envelope between the 5th and 95th percentiles of the model fluxes – an encouraging result. The middle panel of Figure 8 shows the comparison between model and observations at an energy of 5.28 keV. At this energy the model fluxes are less well matched to observations although the measured flux is still found within the envelope between the 5th and 95th percentiles of the model fluxes at almost all times, except during periods when the measured fluxes fall to very low levels. The NRMSD values calculated for the five day period in Figure 8 are 1.895 (13.4 keV) and 2.053 (5.28 keV). As is clear from the plots, these rather high values would be expected to fall significantly should robust inter-calibration between AMC-12/CEASE-II and LANL/MPA were carried out (or even more simply, if a constant value were subtracted from the model values).

It is clear from the data shown in Figure 8 that at times the CEASE-II sensor reports very low flux values, whereas the model results, based on averaged fluxes from LANL/MPA, are almost always higher. Of course, whilst it would be ideal to obtain good agreement between model and data for all flux levels, typically interest is greatest at the highest flux values. In this respect the current model does track the measured flux variations from the AMC-12/CEASE-II observations reasonably well during the period in question.

A further comparison between the model fluxes and the measured fluxes may be carried out by examination of the energy spectra. The measured electron energy spectrum can, and indeed does, change very quickly depending on the prevalent conditions in the magnetosphere. In comparison, the fluxes derived from the model change relatively smoothly, depending on the inputs of Kp and local-time. Despite this, it can be informative to examine the energy spectrum in each case to look for agreements and disagreements in order to determine areas where systematic differences are present. These may indicate periods of time, or certain conditions, during which the model may require modification.

Figure 9 contains a plot of two example electron energy spectra from the CEASE-II instrument during Day 61 of 2013, at local midnight (top panel) and at local noon (bottom panel). The model predictions for these times are shown in red and the measured data are shown in blue. The solid line is the mean from the model and the dashed lines indicate the 5th, 25th, 75th, and 95th, percentiles. It is clear to see that the model fluxes at both noon and midnight vary in a quasi log-linear manner. The fluxes predicted by the model during this period are somewhat higher than those observed in both instances (cf. Figure 8). However, it is also clear that the best match between data and model for the two cases shown in Figure 9 is found at local noon where both the magnitude of the predicted flux level, and the general slope of the spectra, are both reasonably well-matched to observations (mostly within the envelope between the 5th and 95th percentiles). At local midnight the slope of the model spectrum is steeper than that measured by CEASE-II. In addition, the satellite observations at noon and midnight show a local maximum at ~5-10 keV that is not reproduced by the model.

Given that the CEASE-II sensor and the LANL/MPA instrumentation have not been inter-calibrated, the results shown in Figure 8 and Figure 9 are encouraging, and would be likely to improve even further upon intercalibration between the satellites. These results provide independent evidence that this first incarnation of the model can be utilized to make coarse predictions of the plasma flux environment at GEO. Unfortunately, the CEASE-II sensor does not also measure the ion population below 40 keV. It is planned to test the model ion flux predictions against independent observations at GEO in future using other datasets.

4.3 Model limitations

In the current incarnation of the model both the electron and ion flux are predicted at any local-time around Earth, at any specified energy between 1.034 eV and 40.326 keV for electrons, and between 1.816 and 40.649 keV for ions, and at any specified Kp value. The model is not applicable for times when the magnetosheath moves inwards of GEO. In addition, the model does not (yet) include the effects of : (i) substorm dynamics, (ii) substorm injections, or (iii) drift echoes or dispersion features. Any of these three issues may be important for some applications. In addition, since LANL/MPA only measures the fluxes from ~1 eV to ~40 keV then the model can only be used to estimate the partial plasma pressure (and energy-density), rather than the total plasma pressure due to the complete distribution at all energies.

The current model does not provide “confidence limits”, or other goodness-of-fit parameters to the flux values provided. This is intentional. The mean values from the MPA observations are the average value recorded by the instruments over the entire dataset. Along with the standard deviation and the percentiles, these values provide a broad means to gauge the likelihood of both the electron and the ion flux obtaining a particular level. In the opinion of the authors, accurate estimates of uncertainties in the flux values are practically impossible to determine due to (a) the rapidly changing background distribution of the plasma (since the ion and electron distributions at GEO are highly complex, rarely Maxwellian, and evolve rapidly in time), and (b) the dependence of the particle populations upon the time-history of the solar wind and the time-history of the magnetosphere. At present, the probability distributions (see Table 1 and also Figure 3), and the percentiles provided by the model (see Table 2 and also Figures 7, 8, and 9), offer some broad indications of the spread and the variance within the data.

4.4 Model availability and future development

The computer code implemented to perform the binning and the grid interpolation scheme was initially written in the IDL programming language. However, the authors have also produced a FORTRAN version of the code. This version of the code can be easily modified to suit user requirements.

This initial report describes the status of the model in January 2015. The electron flux has been tested against an independent data set and shown to give generally good results during quiet and disturbed periods. Testing of the ion flux predicted by the model against an independent data set has not been carried out to date. We also aim to utilize results from the model to drive simulations of the inner magnetosphere where fluxes from GEO are used as either boundary conditions or are predicted by the model (e.g. *Jordanova et al.* [1998], *Zaharia et al.* [2005; 2006], *Jordanova et al.* [2010b], *Katus et al.* [2014]). Many current models use a limited range of boundary conditions at GEO that do not provide the level of detail with regard to local-time, solar activity, and geomagnetic activity, available in the model described here. Hence, we hope for a marked improvement in the output from future simulations, in comparison with observations, when these new model inputs are utilized.

Another area that is ripe for investigation is development of the model such that it can be driven by incident solar-wind conditions (e.g. the solar wind velocity, V_{SW}, and the magnetic field orientation, IMF-B_z). The magnetospheric system is ultimately driven by the solar-wind, and hence a model driven by upstream solar wind parameters would give better opportunity to *predict* the fluxes at some point in the future (i.e. a model driven by V_{SW} and B_z or similar, e.g. *Hartley et al.*

[2014]). This would contrast with the current model which uses the instantaneous local conditions close to Earth (i.e. proxied by the Kp index). Of course, given the recent progress in the development of improved solar-wind/magnetosphere coupling functions (e.g. *Newell et al.* [2007]; *Borovsky* [2014]; *McPherron et al.* [2015]), one could further envisage development of a version of the model to explore predictions of ion and electron fluxes based on the various coupling functions in use in the community.

5. Summary

1. A new empirical model of the ion flux and the electron flux as a function of local-time, geomagnetic activity, and solar activity, has been developed for geosynchronous orbit for energies between ~1 eV and 40 keV. The electron flux derived from the model has been tested and is generally found to be in reasonably good agreement with independent observations during quiet and disturbed geophysical conditions.

2. The new model provides scientific and operational users with predictions of fluxes for a wider range of input conditions than is generally the case with current models. We intend to pursue both scientific and operational development of the model in future development.

3. A beta-version of the model is freely available as a FORTRAN code that can be adapted to user-requirements.

It is hoped that this model will be found useful by the operational community and the scientific community and we welcome input for how the model could be improved and developed in future.

6. Acknowledgements

The authors gratefully acknowledge the OMNI database for the solar wind and geophysical parameters used in this study. LANL/MPA data and work at LANL were performed under the auspices of the U.S. Department of Energy with support from the Los Alamos Laboratory Directed Research and Development (LDRD) program. MPA data are available by contacting the MPA PI, Mike Henderson, at mghenderson@lanl.gov. A beta-version of the model is available by contacting MHD at mdenton@spacescience.org.

References

Bame, S. J., D. J. McComas, M. F. Thomsen, B. L. Barraclough, R. C. Elphic, J. P. Glore, J. C. Chavez, E. P. Evans and F. J. Wymer, Rev. Sci. Instrum., 64, 1026-1033, 1993.

Bartels, J., N. A. H. Heck, and H. F. Johnstone, The three-hour-range index measuring geomagnetic activity, J. Geophys. Res., 44, 411-454, 1939.

Borovsky, J. E., M. F. Thomsen, and D. J. McComas, The superdense plasma sheet: Plasmaspheric origin, solar wind origin, or ionospheric origin?, J. Geophys. Res., 102(A10), 22089–22097, doi:10.1029/96JA02469, 1997.

Borovsky, J. E., and M. H. Denton, Differences between CME-driven storms and CIR-driven storms, J. Geophys. Res., 111, A07S08, doi:10.1029/2005JA011447, 2006.

Borovsky, J. E., and M. H. Denton, The effect of plasmaspheric drainage plumes on solar-wind/magnetosphere coupling, Geophys. Res. Lett., 33, L20101, 2006.

Borovsky, J. E., and M. H. Denton, A statistical look at plasmaspheric drainage plumes, J. Geophys. Res., 113, A09221, 2008.

Borovsky, J. E., and M. H. Denton, Electron loss rates from the outer electron radiation belt caused by the filling of the outer plasmasphere: The calm before the storm, J. Geophys. Res., 114, A11203, 2009.

Borovsky, J. E., M. H. Denton, R. E. Denton, V. K. Jordanova, and J. Krall, Estimating the Effects of Ionospheric Plasma on Solar-Wind/Magnetosphere Coupling Via Mass Loading of Dayside Reconnection: Ion-Plasma-Sheet Oxygen, Plasmaspheric Drainage Plumes, and the Plasma Cloak, J. Geophys. Res., 118, 5695, 2013.

Borovsky, J. E., D. T. Welling, M. F. Thomsen, and M. H. Denton, Long-lived plasmaspheric drainage plumes: Where does the plasma come from?, J. Geophys. Res., (*in press*) 2014.

Borovsky, J. E., Physical improvements to the solar wind reconnection control function for the Earth's magnetosphere, J. Geophys. Res. Space Physics, 118, 2113–2121, doi:10.1002/jgra.50110, 2013.

Borovsky, J. E., M. F. Thomsen, and D. J. McComas, The superdense plasma sheet: Plasmaspheric origin, solar wind origin, or ionospheric origin?, J. Geophys. Res., 102, 22089-22097, 1997.

Denton, M. H., and J. E. Borovsky, Observations and modeling of magnetic flux tube refilling at geosynchronous orbit, J. Geophys. Res., (in press) 2014.

Denton, M. H., and J. E. Borovsky, The superdense plasma sheet in the magnetosphere during high-speed-stream-driven storms: plasma transport and timescales, J. Atmos. Sol-Terr. Phys., 71, 1045-1058, 2009.

Denton, M. H., and J. E. Borovsky, Magnetosphere response to high-speed solar-wind streams: A comparison of weak and strong driving and the importance of extended periods of fast solar wind, J. Geophys. Res., 117, A00L05, doi:10.1029/2011JA017124, 2012.

Denton, M. H., M. F. Thomsen, B. Lavraud, M. G. Henderson, R. M. Skoug, H. O. Funsten, J.-M. Jahn, C. J. Pollock, and J. M. Weygand, Transport of plasma sheet material to the inner magnetosphere, Geophys. Res. Lett., 34, L04105, doi:10.1029/2006GL027886, 2007.

Denton, M. H., M. F. Thomsen, H. Korth, S. Lynch, J. C. Zhang and M. W. Liemohn, Bulk plasma properties at geosynchronous orbit, J. Geophys. Res., 110, A07223, 2005.

Dichter, B. K., J. 0. McGarity, M. R. Oberhardt, V. T. Jordanov, D. J. Sperry, A. C. Huber, J. A. Pantazis, E. G. Mullen, G. Ginet, and M. S. Gussenhoven, Compact Environmental Anomaly Sensor (CEASE): A novel spacecraft instrument for in situ measurements of environmental conditions, IEEE Trans. Nucl. Sci., 45, 2758–2764, 1998.

Elphic, R. C., L. A. Weiss, M. F. Thomsen, D. J. McComas, and M. B. Moldwin, Evolution of plasmaspheric ions at geosynchronous orbit during times of high geomagnetic activity, Geophys. Res. Lett., 23, 2189, 1996.

Ganushkina, N. Y., O. A. Amariutei, D. Welling, and D. Heynderickx, Nowcast model for low-energy electrons in the inner magnetosphere, Space Weather, 13, 16–34, doi:10.1002/2014SW001098, 2015.

Ganushkina, N. Y., M. W. Liemohn, O. A. Amariutei, and D. Pitchford, Low-energy electrons (5–50 keV) in the inner magnetosphere, J. Geophys. Res. Space Physics, 119, 246–259, doi:10.1002/2013JA019304, 2014.

Ganushkina, N. Y., O. Amariutei, Y. Y. Shpritz, and M. Liemohn, Transport of the plasma sheet electrons to the geostationary distances, J. Geophys. Res. Space Physics, 118, 82–98, doi:10.1029/2012JA017923, 2013.

Ginet, G. P., T. P. O'Brien, S. L. Huston, W. R. Johnston, T. B. Guild, R. Friedel, C. D. Lindstrom, C. J. Roth, P. Whelan, R. A. Quinn, D. Madden, S. Morley, and Yi-Jiun Su, AE9, AP9 and SPM: New Models for Specifying the Trapped Energetic Particle and Space Plasma Environment, in The Van Allen Probes mission, eds N. Fox and J. L. Burch, Springer, doi:10.1007/978-1-4899-7433-4, ISBN: 978-1-4899-7432-7, 2014.

Goldstein, J., B. R. Sandel, M. F. Thomsen, M. Spasojevic, and P. H. Reiff, Simultaneous remote sensing and in situ observations of plasmaspheric drainage plumes, J. Geophys. Res., 109, A03202, 2004.

Hartley, D. P., M. H. Denton, and J. V. Rodriguez, Electron number density, temperature, and energy density at GEO and links to the solar wind: A simple predictive capability, J. Geophys. Res. Space Physics, 119, 4556–4571, doi:10.1002/2014JA019779, 2014.

Henderson, M. G., R. Skoug, E. Donovan, M. F. Thomsen, G. D. Reeves, M. H. Denton, H. J. Singer, R. L. McPherron, S. B. Mende, T. J. Immel, J. B. Sigwarth and L. A. Frank, Substorms during the August 10-11 sawtooth event, J. Geophys. Res., 111, A06206, 2006b.

Henderson, M. G., G. D. Reeves, R. Skoug, M. F. Thomsen, M. H. Denton, S. B. Mende, T. J. Immel, P. C. Brandt and H. Singer, Magnetospheric and auroral activity during the April 18, 2002 sawtooth event, J. Geophys., 111, A01S90, 2006a.

Huddleston, M. M., C. R. Chappell, D. C. Delcourt, T. E. Moore, B. L. Giles, and M. O. Chandler, An examination of the process and magnitude of ionospheric plasma supply to the magnetosphere. J. Geophys. Res., 110. doi:10.1029/2004JA010401, 2005.

Jordanova, V. K., S. Zaharia, and D. T. Welling, Comparative study of ring current development using empirical, dipolar, and self-consistent magnetic field simulations, J. Geophys. Res., 115, A00J11, doi:10.1029/2010JA015671, 2010b.

Jordanova, V. K., C. J. Farrugia, L. Janoo, J. M. Quinn, R. B. Torbert, K. W. Ogilvie, R. P. Lepping, J. T. Steinberg, D. J. McComas, and R. D. Belian, October 1995 magnetic cloud and accompanying storm activity: Ring current evolution, J. Geophys. Res., 103, 79, 1998.

Jordanova, V. K., L. M. Kistler, M. F. Thomsen, and C. G. Mouikis, Effects of plasma sheet variability on the fast initial ring current decay, Geophys. Res. Lett., 30(6), 1311, doi:10.1029/2002GL016576, 2003.

Jordanova, V. K., R. M. Thorne, W. Li , Y. Miyoshi, Excitation of whistler mode chorus from global ring current simulations, J. Geophys. Res., 115, A00F10, doi:10.1029/2009JA014810, 2010a.

Katus, R. M., M. W. Liemohn, E. L. Ionides, R. Ilie, D. Welling, and L. K. Sarno-Smith, Statistical analysis of the geomagnetic response to different solar wind drivers and the dependence on storm intensity, J. Geophys. Res., doi:10.1002/2014JA020712, 2014.

Korth, H., M. F. Thomsen, J. E. Borovsky, and D. J. McComas, Plasma sheet access to geosynchronous orbit, J. Geophys. Res., 104, 25,047–25,061, 1999.

Korth, H., and M. F. Thomsen, Plasma sheet access to geosynchronous orbit: Generalization to numerical global field models, J. Geophys. Res., 106(A12), 29655–29667, doi:10.1029/2000JA000373, 2001.

Kronberg, E. A., Ashour-Abdalla, M., Dandouras, I., Delcourt, D. C., Grigorenko, E. E., Kistler, L. M., ... Zelenyi, L. M., Circulation of Heavy Ions and Their Dynamical Effects in the Magnetosphere: Recent Observations and Models. Space Science Reviews, 184(1-4), 173-235. doi:10.1007/s11214-014-

0104-0, 2014.

Lawrence, D. J., M. F. Thomsen, J. E. Borovsky, and D. J. McComas, Measurements of early and late-time plasmasphere refilling as observed from geosynchronous orbit, J. Geophys. Res., 104, 14691, 1999.

McPherron, R.L., X. Chu, and T.-S. Hsu, An Optimum Solar Wind Coupling Function for the AL Index, J. Geophys. Res., submitted Sept 2014.

MacDonald, E. A., L. W. Blum, S. P. Gary, and M. H. Denton., Superposed epoch analysis of a whistler instability criterion at geosynchronous orbit during geomagnetic storms, Proc. Roy. Soc. A, 466, 3351-3362, doi:10.1098/rspa.2010.0076, 2010.

MacDonald, E. A., M. H. Denton, M. F. Thomsen, and S. P. Gary, High-speed stream driven inferences of global wave distributions at geosynchronous orbit; relevance to radiation belt dynamics, J. Atmos. Sol-Terr. Phys., 70, 1789-1796, doi:10.1016/j.jastp.2008.03.021, 2008.

Mauk, B. H., and C.-I. Meng, Characterization of geostationary particle signatures based on the ‘Injection Boundary’ Model, J. Geophys. Res., 88(A4), 3055–3071, doi:10.1029/JA088iA04p03055, 1983.

Mouikis, C. G., L. M. Kistler, Y. H. Liu, B. Klecker, A. Korth, and I. Dandouras, H^+ and O^+ content of the plasma sheet at 15-19 R_e as a function of geomagnetic and solar activity, J. Geophys. Res., 115, A00J16. doi:10.1029/2010JA015978, 2010.

Newell, P. T., T. Sotirelis, K. Liou, C.-I. Meng, and F. J. Rich, A nearly universal solar wind-magnetosphere coupling function inferred from 10 magnetospheric state variables, J. Geophys. Res., 112, A01206, doi:10.1029/2006JA012015, 2007.

Nosé, M., R. W. McEntire, and S. P. Christon, Change of the plasma sheet ion composition during magnetic storm development observed by the Geotail spacecraft, J. Geophys. Res., 108(A5), 1201. doi:10.1029/2002JA009660, 2003.

Purvis, C. K., H. B. Garrett, A. C. Whittlesey, and N. J. Stevens, Design guidelines for assessing and controlling spacecraft charging effects, NASA Tech. Pap. 2361, 1984.

Sandel, B. R., and M. H. Denton, Global view of refilling of the plasmasphere, Geophys. Res. Lett., 34, L17102, 2007.

Sicard-Piet, A., S. Bourdarie, D. Boscher, R. H. W. Friedel, M. Thomsen, T. Goka, H. Matsumoto, and H. Koshiishi, A new international geostationary electron model: IGE-2006, from 1 keV to 5.2 MeV, Space Weather, 6, S07003, doi:10.1029/2007SW000368, 2008.

Thomsen, M. F., E. Noveroske, J. E. Borovsky, and D. J. McComas, Calculating the Moments from Measurements by the Los Alamos Magnetospheric Plasma Analyzer, LA-13566-MS, Los Alamos National Laboratory, 1999.

Thomsen, M. F., D. J. McComas, J. E. Borovsky, and R. C. Elphic, The magnetospheric trough, in Geospace Mass and Energy Flows, Geophys. Monograph. Ser., 104, edited by J. Horwitz, D. L. Gallagher, and W. K. Peterson, p355, AGU, 1998.

Thomsen, M. F., Why Kp is such a good measure of magnetospheric convection, Space Weather, 2, S11004, doi:10.1029/2004SW000089, 2004.

Thomsen, M. F., M. H. Denton, B. Lavraud, and M. Bodeau, Statistics of plasma fluxes at geosynchronous orbit over more than a full solar cycle, Space Weather, 5, S03004, doi:10.1029/2006SW000257, 2007.

Thomsen, M. F., J. E. Borovsky, R. M. Skoug, and C. W. Smith, Delivery of cold, dense plasma sheet material into the near-Earth region, J. Geophys. Res., 108, 1151, doi:10.1029/2002JA009544, A4, 2003.

Thomsen, M. F., J. Birn, J. E. Borovsky, K. Morzinski, D. J. McComas, and G. D. Reeves, Two-satellite observations of substorm injections at geosynchronous orbit, J. Geophys. Res., 106(A5), 8405–8416, doi:10.1029/2000JA000080, 2001.

Thomsen, M. F., J. E. Borovsky, D. J. McComas, and M. R. Collier, Variability of the ring current source population, Geophys. Res. Lett., 25, 3481-3484, 1998.

Weiss, L. A., R. L. Lambour, R. C. Elphic, and M. F. Thomsen, Study of plasmaspheric evolution using geosynchronous observations and global modeling, Geophys Res. Lett., 24, 599, 1997.

Welling, D. T., & Ridley, A. J., Exploring sources of magnetospheric plasma using multispecies MHD. Journal of Geophysical Research, 115(A4), A04201. doi:10.1029/2009JA014596, 2010.

Yau, A. W., and M. André, Sources of Ion Outflow in the High Latitude Ionosphere, Space Sci. Rev., 80, 1-25. doi:10.1023/A:1004947203046, 1997.

Zaharia, S., M. F. Thomsen, J. Birn, M. H. Denton, V. K. Jordanova, and C. Z. Cheng, Effect of storm-time plasma pressure on the magnetic field in the inner magnetosphere, Geophys. Res. Lett., 32, L03102, doi:10.1029/2004GL021491, 2005.

Zaharia, S., V. K. Jordanova, M. F. Thomsen, and G. D. Reeves, Self-consistent modeling of magnetic fields and plasmas in the inner magnetosphere: Application to a geomagnetic storm, J. Geophys. Res., 111, A11S14, doi:10.1029/2006JA011619, 2006.

Table 1. Statistical parameters of the electron flux and ion flux distributions shown in Figure 3.

	Electron (17923 eV)	**Ions (18276 eV)**
Mean	2.177	2.020
Standard Deviation	0.594	0.336
Variance	0.352	0.113
Skewness	0.609	-0.407
Kurtosis	-0.071	0.586
	Electron (4639 eV)	**Ions (4822 eV)**
Mean	3.013	2.122
Standard Deviation	0.711	0.393
Variance	0.505	0.154
Skewness	0.060	-0.642
Kurtosis	-0.709	1.319
	Electron (309.0 eV)	**Ions (335.7 eV)**
Mean	4.028	2.554
Standard Deviation	0.556	0.332
Variance	0.309	0.110
Skewness	-0.573	-0.397
Kurtosis	0.472	1.551

Table 2. Example model outputs for Kp=3 and 18.00 LT.

ALL F10.7							
ELECTRONS	**Mean**	**Std. Dev**	**5%**	**25%**	**Median**	**75%**	**95%**
100 eV	4.0989	0.5651	3.1531	3.6227	4.1713	4.5632	4.9165
500 eV	3.3031	0.5943	2.4298	2.7630	3.3051	3.8483	4.2203
1 keV	2.81791	0.5528	2.1080	2.3545	2.7196	3.2060	3.8330
10 keV	1.6719	0.4380	1.0333	1.4934	1.7370	1.9319	2.1453
30 keV	1.3870	0.3021	0.8991	1.2927	1.4403	1.5772	1.7011
IONS	**Mean**	**Std. Dev**	**5%**	**25%**	**Median**	**75%**	**95%**
100 eV	2.7920	0.3092	2.1902	2.6156	2.8263	3.0106	3.2148
500 eV	2.2406	0.3049	1.6188	2.0981	2.2993	2.4444	2.6393
1 keV	2.0298	0.3916	1.3527	1.9369	2.1064	2.2473	2.4060
10 keV	2.1832	0.2113	1.9126	2.0274	2.1248	2.3173	2.6064
30 keV	2.0004	0.1831	1.7643	1.8878	1.9610	2.0704	2.3914
F10.7 < 100							
ELECTRONS	**Mean**	**Std. Dev**	**5%**	**25%**	**Median**	**75%**	**95%**
100 eV	4.0647	0.5647	3.2207	3.5847	4.0620	4.5435	4.9584
500 eV	3.2766	0.5982	2.4426	2.7556	3.2557	3.7673	4.2696
1 keV	2.8090	0.5634	2.1188	2.3615	2.6840	3.1346	3.8914
10 keV	1.7197	0.4622	0.9851	1.5896	1.7789	1.9669	2.1668
30 keV	1.3795	0.3102	0.8991	1.3035	1.4324	1.5513	1.6930
IONS	**Mean**	**Std. Dev**	**5%**	**25%**	**Median**	**75%**	**95%**
100 eV	2.8157	0.3111	2.1902	2.6644	2.8598	3.0328	3.2156
500 eV	2.2548	0.3079	1.6188	2.1301	2.3204	2.4508	2.6297
1 keV	2.0255	0.4153	1.3527	1.9369	2.1199	2.2490	2.4057
10 keV	2.1650	0.2159	1.8967	2.0071	2.0975	2.3132	2.5778
30 keV	1.9744	0.1809	1.7363	1.8708	1.9365	2.0454	2.3937
100 ≤ F10.7 < 170							
ELECTRONS	**Mean**	**Std. Dev**	**5%**	**25%**	**Median**	**75%**	**95%**
100 eV	4.1874	0.5457	3.2393	3.7983	4.1890	4.6598	4.9700
500 eV	3.3281	0.6042	2.2808	2.9035	3.3487	3.7574	4.3402
1 keV	2.7516	0.5192	2.0378	2.4094	2.6205	3.0626	3.8758
10 keV	1.8760	0.3663	1.2375	1.7101	1.8976	2.0936	2.3870
30 keV	1.5401	0.2482	1.1675	1.4492	1.5767	1.6894	1.8202
IONS	**Mean**	**Std. Dev**	**5%**	**25%**	**Median**	**75%**	**95%**
100 eV	2.9447	0.3565	2.4823	2.7912	2.9728	3.1395	3.3458
500 eV	2.4065	0.2652	1.9148	2.2937	2.4493	2.5851	2.7317
1 keV	2.2265	0.3334	1.8010	2.1176	2.2598	2.3879	2.5560
10 keV	2.2845	0.2780	1.9554	2.0942	2.2425	2.3959	3.0312
30 keV	2.0819	0.1686	1.8105	1.9583	2.0939	2.1894	2.3600
F10.7 ≥ 170							
ELECTRONS	**Mean**	**Std. Dev**	**5%**	**25%**	**Median**	**75%**	**95%**
100 eV	4.2164	0.5411	3.2335	3.8584	4.3157	4.6751	4.9700
500 eV	3.2933	0.5387	2.4298	2.8590	3.2597	3.6800	4.1949
1 keV	2.8417	0.4969	2.2192	2.4312	2.7720	3.1239	3.8549
10 keV	2.0339	0.3826	1.3307	1.7094	1.9906	2.2612	2.5596
30 keV	1.5769	0.2283	1.1103	1.4174	1.6135	1.7346	1.8267
IONS	**Mean**	**Std. Dev**	**5%**	**25%**	**Median**	**75%**	**95%**
100 eV	2.8661	0.2966	2.3162	2.7095	2.8901	3.0766	3.2785
500 eV	2.3663	0.4859	1.9321	2.2468	2.4165	2.5617	2.7399
1 keV	2.2262	0.2581	1.7467	2.0899	2.2483	2.3909	2.6214
10 keV	2.3214	0.2062	2.0507	2.1656	2.2651	2.4822	2.7288
30 keV	2.0415	0.1489	1.7619	1.9585	2.0699	2.1424	2.2352

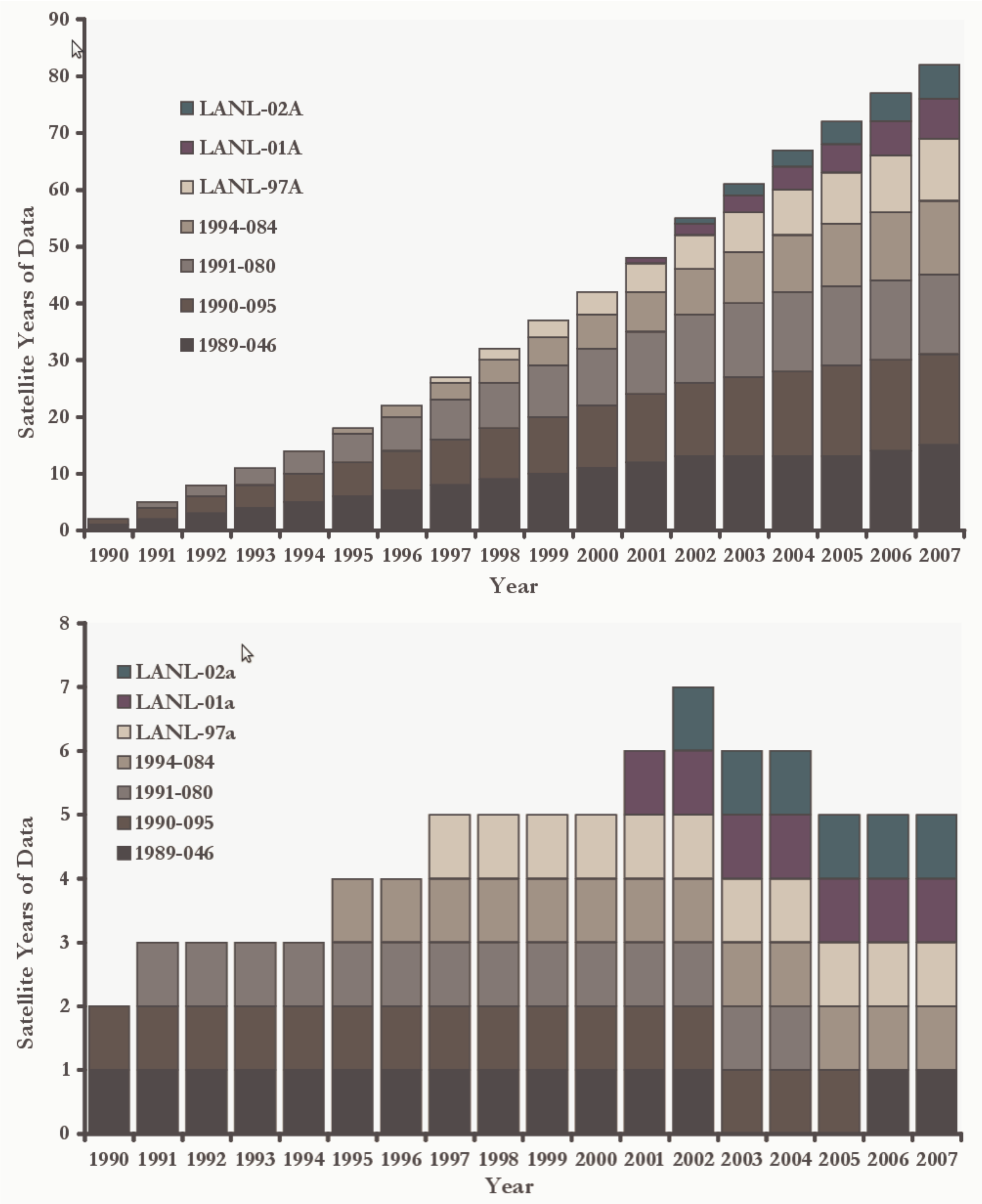

Figure 1. The cumulative amount of LANL/MPA data (in satellite-years) as a function of year, from seven satellites at GEO, between 1990 and 2007 inclusive (top panel). Also the coverage of LANL/MPA in each year from 1990 to 2007 (bottom panel). A total of ~82 satellite-years of data are utilized in the current study)

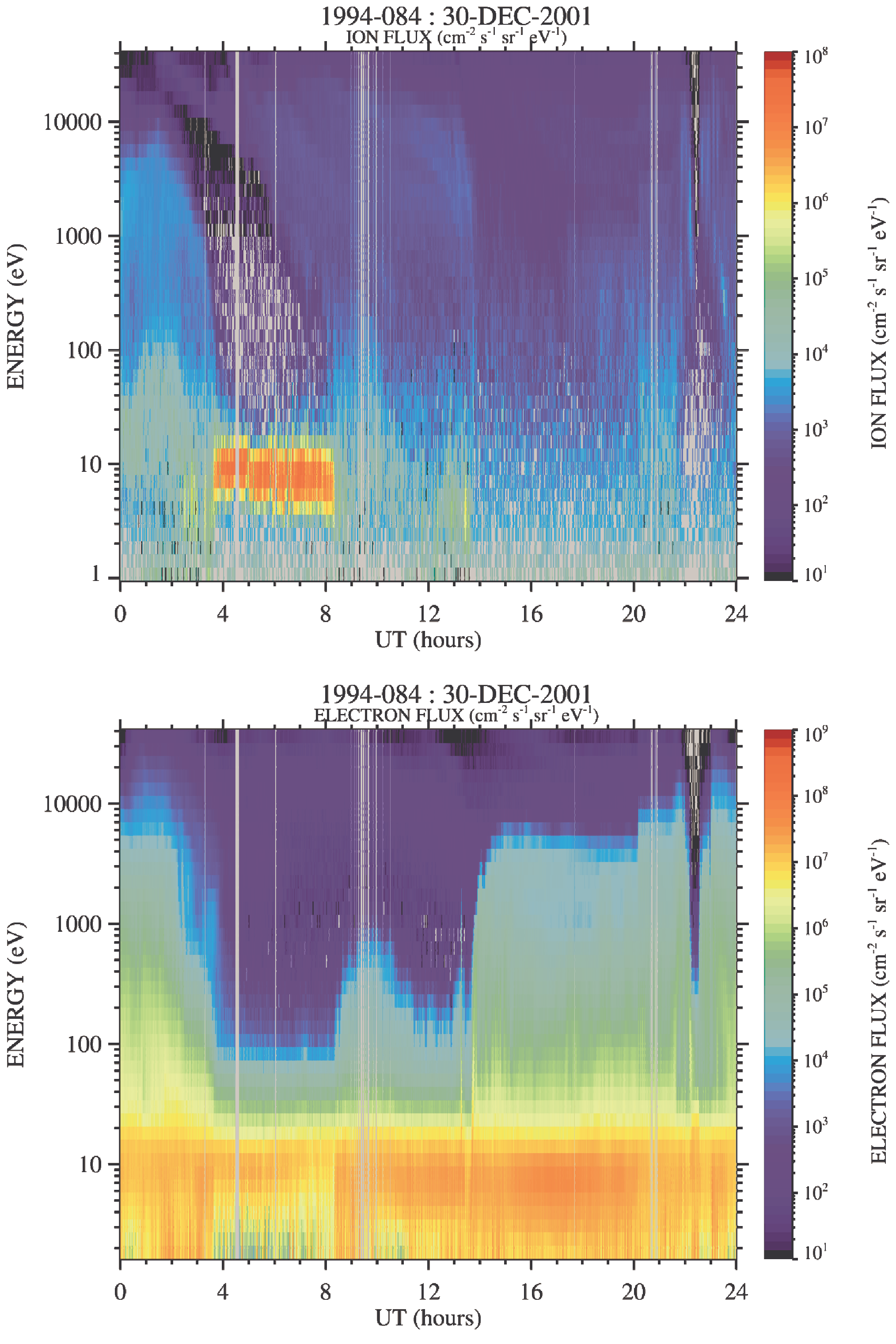

Figure 2. Spectragrams of the fluxes measured by LANL/MPA 1994-084 on 30th Dec 2001. The top panel shows the ion flux. Note the distinctive thermal population (< 1 eV) accelerated through the negative spacecraft potential to ~10 eV between ~4 and 8 UT - a plasmaspheric plume. For most of the rest of the day the spacecraft resides in the ion plasma sheet. The bottom panel shows the electron flux with the spacecraft residing in a electron plasma sheet prior to ~4 UT and after ~8 UT.

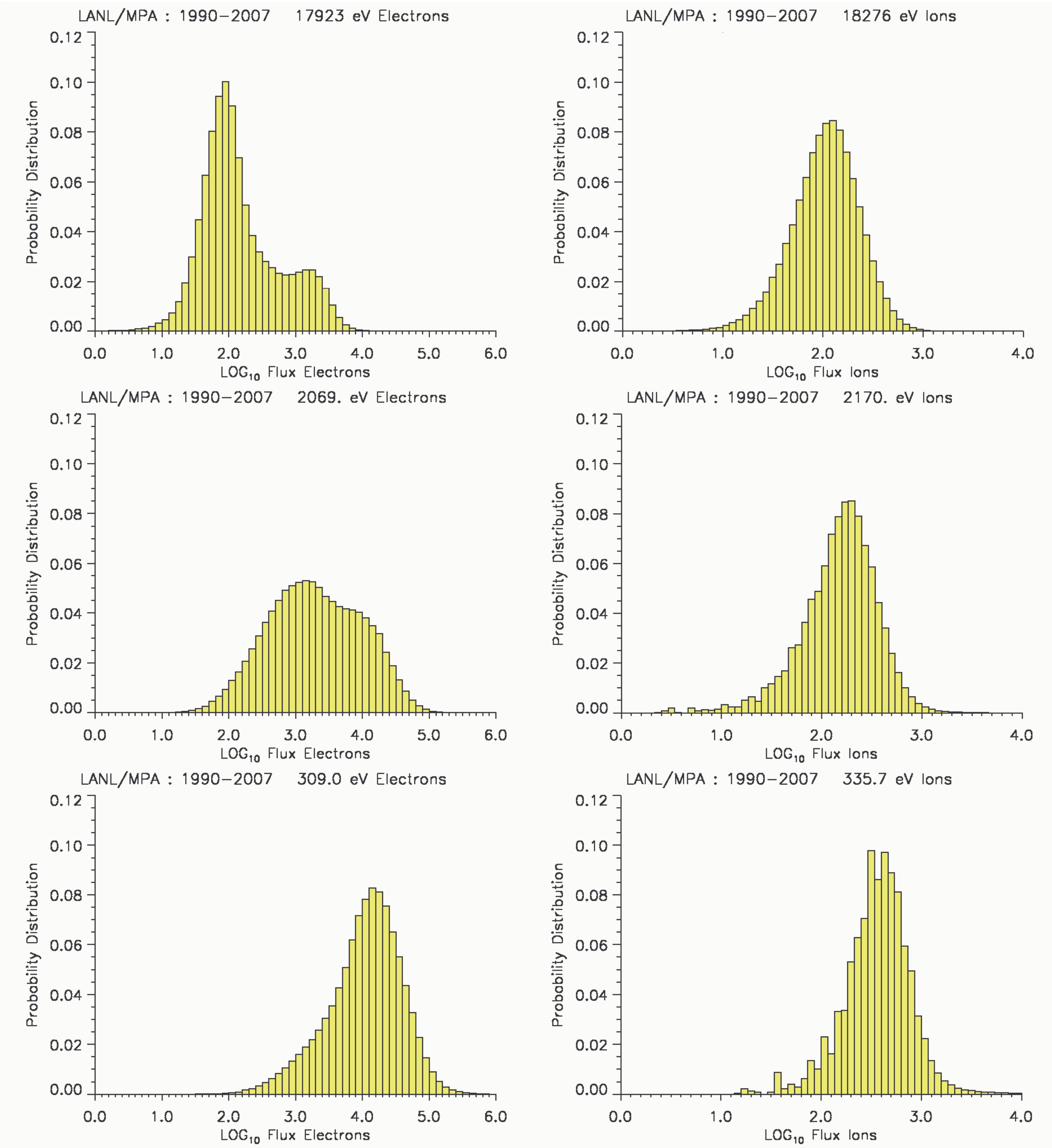

Figure 3. The probability distribution of the electron flux (left column) and the ion flux (right column) measured by three energy-channels (~18 keV, ~2 keV, and ~100 eV) of the LANL/MPA instruments. The distributions are for the entire MPA dataset of seven satellites at GEO between 1990 and 2007 (excluding magnetosheath intervals and intervals of strong spacecraft charging).

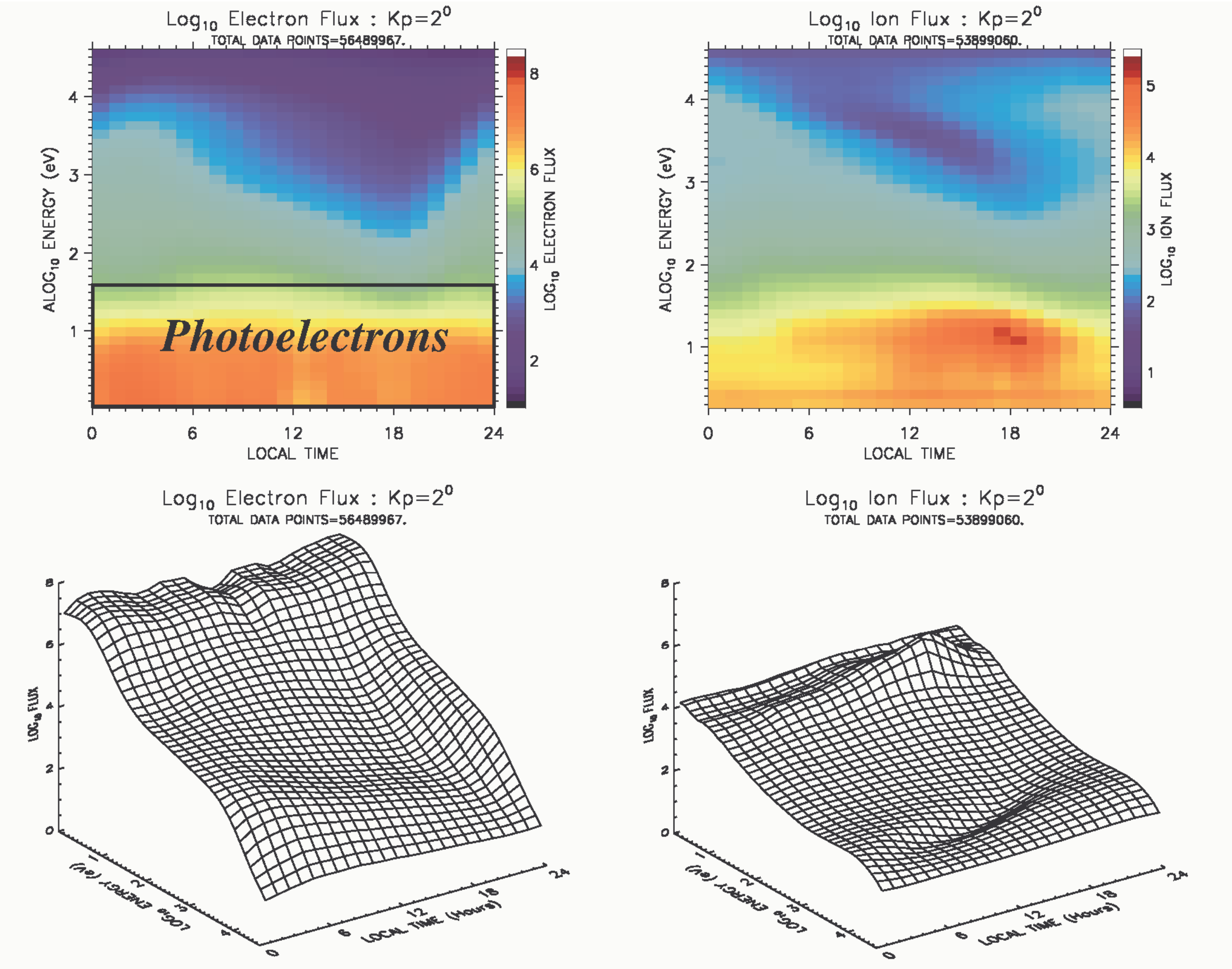

Figure 4. Examples of the mean electron flux and mean ion flux as a function of local-time and energy at a single value of the Kp index (Kp=2). The top row shows a color representation of the fluxes, and the bottom row shows a three-dimensional surface fit. The mean electron flux for energies below ~40 eV should be disregarded.

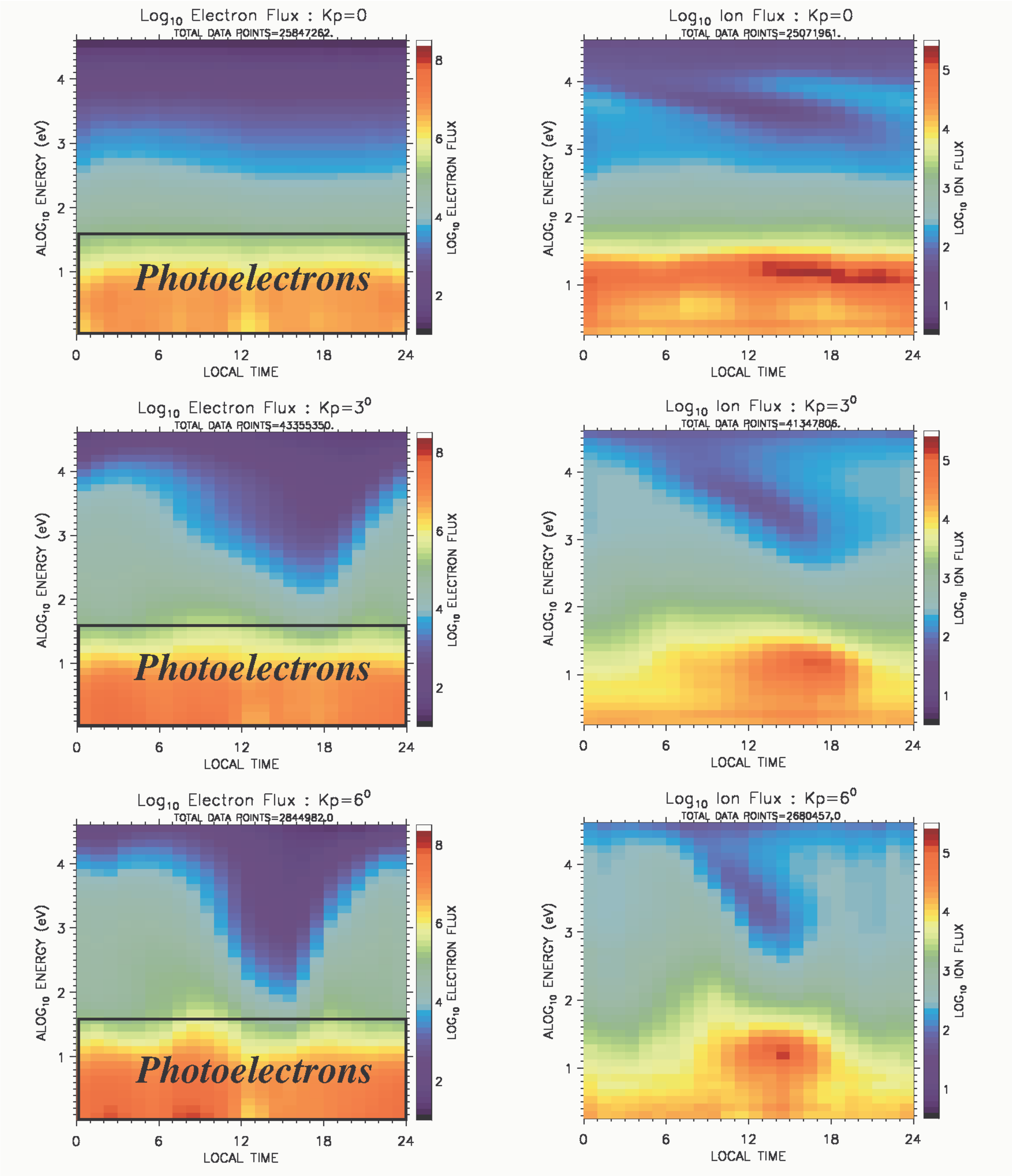

Figure 5. The averaged electron flux (left column) and the averaged ion flux (right column) as a function of energy and local-time at three different values of the Kp index (Kp=0, Kp=3, and Kp=6). The mean electron flux for energies below ~40 eV should be disregarded.

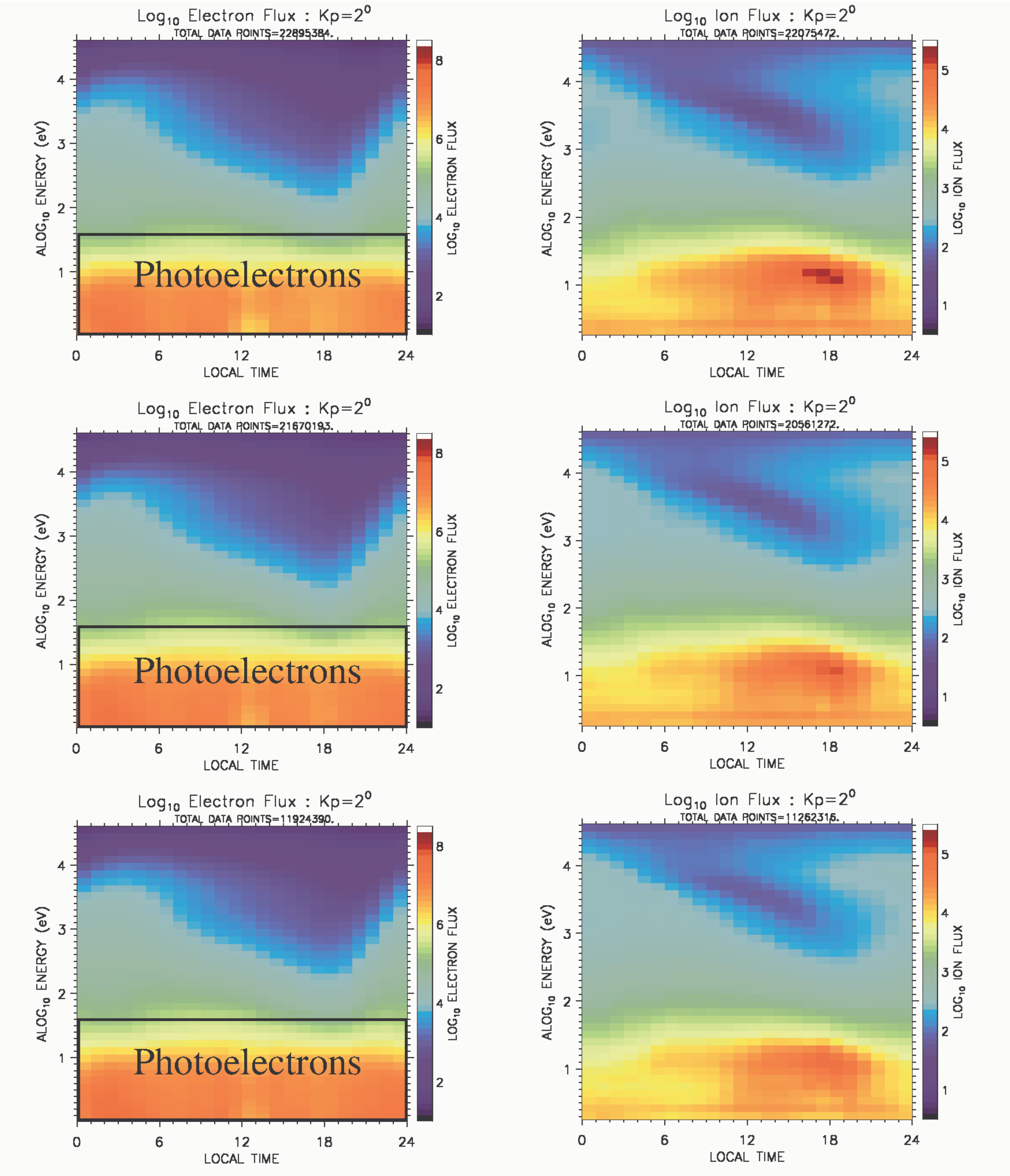

Figure 6. The averaged electron flux (left column) and the averaged ion flux (right column) as a function of energy and local-time, at a fixed value of Kp=2, for three different ranges of F10.7. The top row shows the fluxes for F10.7<100, the middle row for 100≤F10.7<170, and the bottom row for F10.7≥170. The mean electron flux for energies below ~40 eV should be disregarded.

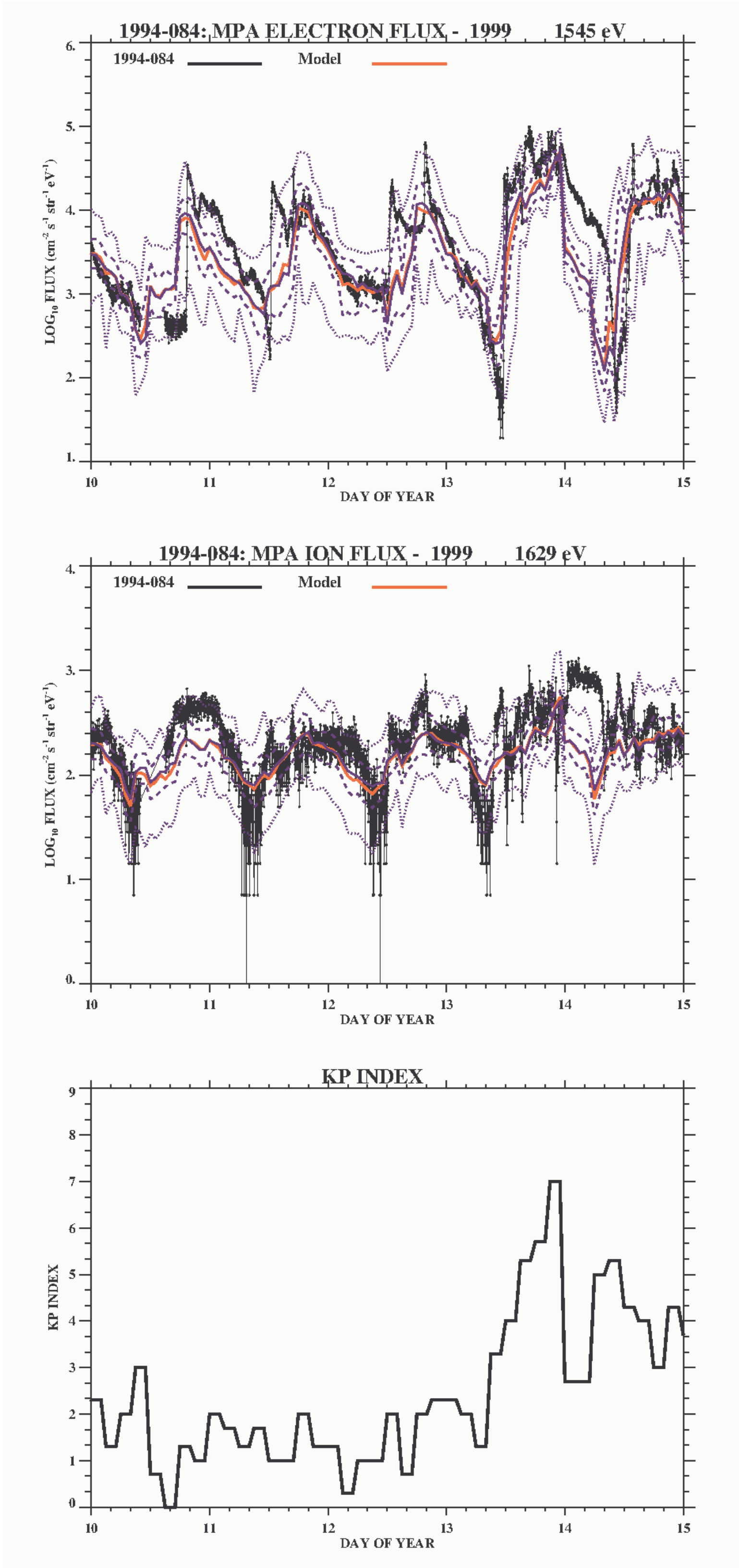

Figure 7. Showing a comparison of the model output with observations from the MPA instrument on satellite 1994-084, during a 5 day period in 1999. The top panel shows the measured electron flux at 1.545 keV. The solid red line is the mean and the solid blue line is the median. The 5th, 25th, 75th and 95th percentiles are also shown (blue dashed lines). The middle panel shows ion observations 1.629 keV in the same format. The Kp index is shown in the bottom panel.

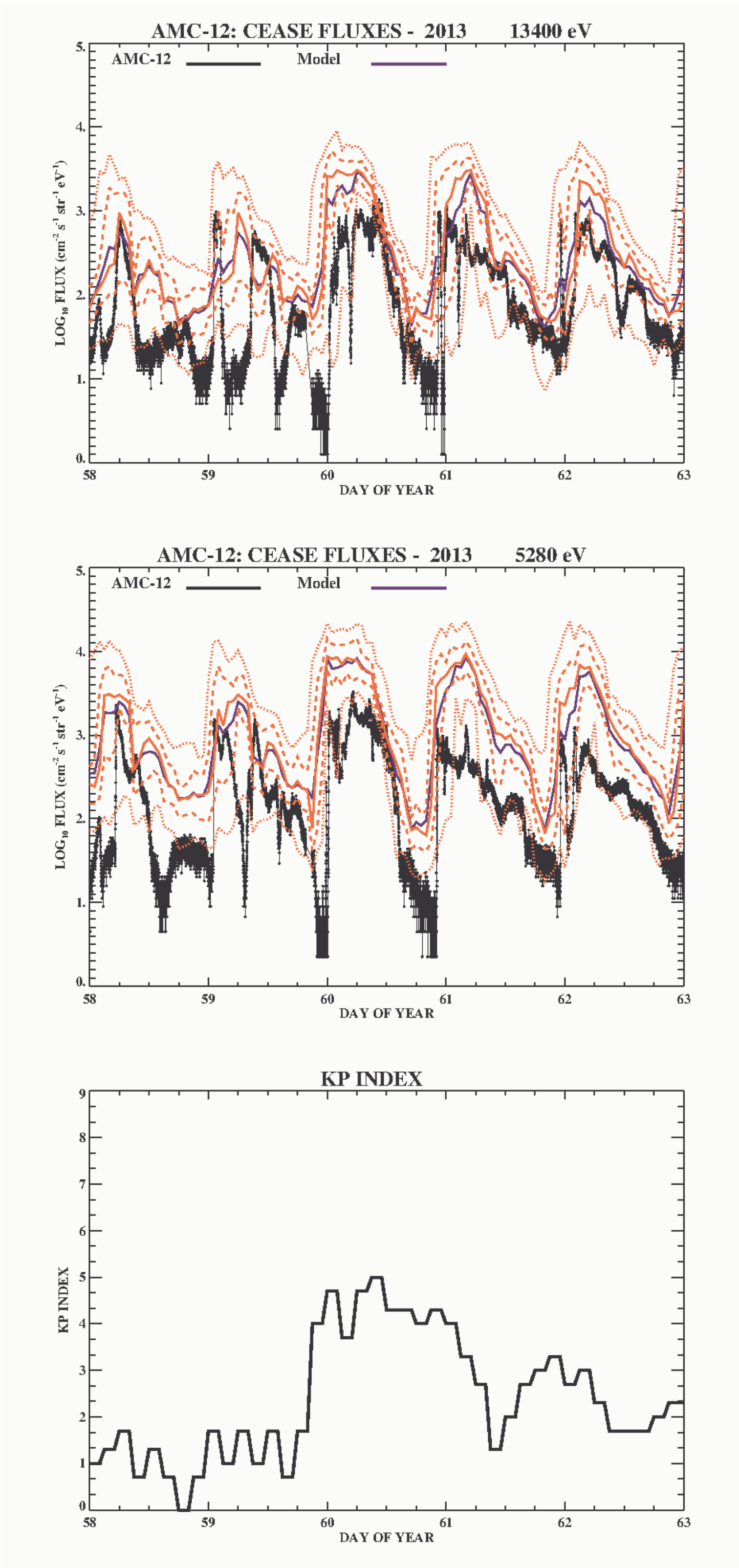

Figure 8. Showing a comparison of the model output with electron observations at 13.40 keV (top panel) and 5.28 keV (middle panel) measured by the CEASE-II instrument package on AMC-12, during a 5 day period in 2013. The black line shows the measured flux, the blue line shows the mean model flux and the red line shows the median. The 5th, 25th, 75th and 95th percentiles are also shown (red dashed lines). The Kp index is shown in the bottom panel.

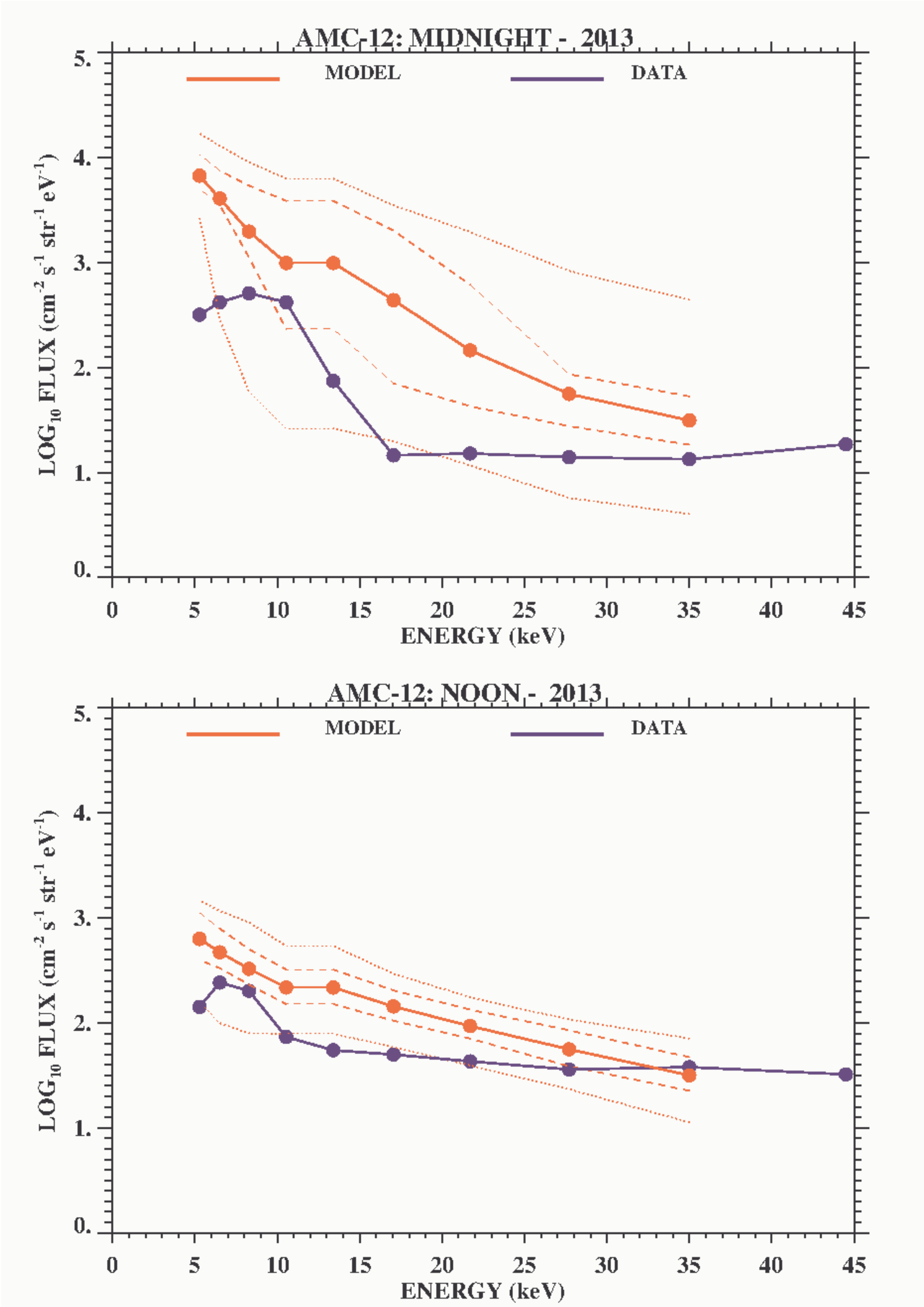

Figure 9. Showing example spectra from the model output (red lines), and from the CEASE-II instrument (blue lines), on day 61 of 2013. The solid red line is the mean and the dashed lines are the 5th, 25th, 75th and 95th percentiles output from the model. The circles indicate the spectra at local midnight (when Kp=4) and the crosses indicate the spectra at local noon (when Kp=2). In this instance, the spectra are much better matched at noon than at midnight.